

# Front page

## Exam information

NFYK10020E - Physics Thesis 60 ECTS, Niels Bohr  
Institute - Contract:134725 (Frederik Bay Nielsen)

## Handed in by

Frederik Bay Nielsen  
dvj107@alumni.ku.dk

## Exam administrators

Eksamensteam, tel 35 33 64 57  
eksamen@science.ku.dk

## Assessors

Heloisa Nunes Bordallo  
Examiner  
bordallo@nbi.ku.dk  
☎ +4535321215

Brian Kjærgaard Hansen  
Co-examiner  
brian@cfm.au.dk

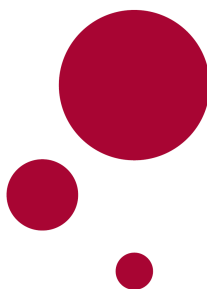
## Hand-in information

**Title:** Delay map modeling in a long-axial field-of-view PET/CT scanner

**Title, english:** Delay map modeling in a long-axial field-of-view PET/CT scanner

**The sworn statement:** Yes

**Does the hand-in contain confidential material:** No



UNIVERSITY OF COPENHAGEN

Faculty of Science

Quantum Physics

MASTER THESIS

# Delay map modeling in a long-axial field-of-view PET/CT scanner

*Frederik Bay Nielsen*

*(KU-id: dvj107)*

**Supervised by**

Heloisa Nunes Bordallo, *University of Copenhagen*

Thomas Lund Andersen, *Rigshospitalet*

Flemming Littrup Andersen, *Rigshospitalet*

May 22<sup>nd</sup>, 2023



## Abstract

Based on dynamic whole-body PET scans of 15 patients receiving one of three tracers:  $[^{15}\text{O}]\text{H}_2\text{O}$ ,  $[^{18}\text{F}]\text{FDG}$  or  $[^{64}\text{Cu}]\text{Cu-DOTATATE}$ , a single voxel delay-finding algorithm is developed which is robust to noise and detects the presence of radiotracer by way of fitting the time activity curve. The map produced is applied as a delay correction method between the voxel time activity curves and the image-derived input function. 21 patients scanned with  $[^{15}\text{O}]\text{H}_2\text{O}$  as the tracer separated into two groups and blood flow in the brain and thyroid was modeled using a one-tissue compartmental model. An organ-specific effect on blood could be observed with a decrease of around  $-40\%$  in the thyroid ( $p \approx 0.002$ ) and no significant change in the brain; Diamox had an increasing effect on the brain blood flow of around  $+40\%$  ( $p < 0.0006$ ) with no significant change in the thyroid. The new single-voxel delay correction method appear to remove a bias related to the conventional method of delay correcting by the mean organ TAC.



## Acknowledgments

I would like to express my grateful appreciation to my supervisor, Heloisa N. Bordallo, at the University of Copenhagen for her invaluable assistance throughout the process of finding this research project. Her dedication as well as her insightful and constructive feedback on my work has been a great help throughout this project. She has been a constant source of motivation throughout the entire process and has been committed to promoting a comfortable work environment that encourages discussion among other students in the research group.

I am also deeply grateful to my supervisors at Rigshospitalet, Thomas L. Andersen and Flemming L. Andersen, for their enthusiasm to share their knowledge and expertise in this field with me, always giving insightful and illuminating answers to my questions, and in particular, their encouragement and dedication which promoted the direction and shaping of my work. It has been a pleasure working with them!

Special thanks also go to Ulrich Lindberg, Rigshospitalet, who has contributed with insightful discussions and new perspectives on the results.

I would like to extend my thanks to the study group at the university, whose presence and constructive suggestions during our regular meetings, as well as in the office space, improved my academic experience, and helped me overcome some of the challenges during the project, in addition to showing their interest in this work.

To all those mentioned above, and to anyone else who may have contributed in any way that cannot be mentioned here, I am very thankful. Everyone's support, guidance, and encouragement have been very valuable to me, and I am truly grateful for the opportunity to have worked with these amazing and inspiring people.



# Contents

<b>Abstract</b>	<b>i</b>
<b>Acknowledgments</b>	<b>ii</b>
<b>1 Introduction</b>	<b>1</b>
1.1 Tracers used in this project . . . . .	2
1.2 Using dynamic PET scans to study kinetics . . . . .	4
1.3 The advantage of long-axial field-of-view PET scanners . . . . .	6
1.4 Aim of the project . . . . .	7
<b>2 Theory</b>	<b>8</b>
2.1 Compartmental modeling . . . . .	8
<b>3 Methods</b>	<b>10</b>
3.1 Setup . . . . .	10
3.2 Data acquisition . . . . .	11
3.3 Delay map algorithm . . . . .	13
3.4 Modeling flow using compartmental modeling . . . . .	18
3.5 Comparing the resulting flow between the two delay correction methods .	18
3.6 Organ segmentation . . . . .	19
<b>4 Results</b>	<b>20</b>
4.1 Delay map . . . . .	20
4.2 Comparison of delay correction methods . . . . .	22



4.3 Results from flow modeling . . . . .	24
<b>5 Discussion</b>	<b>27</b>
<b>6 Future prospects</b>	<b>30</b>
<b>7 Conclusion</b>	<b>31</b>
<b>Bibliography</b>	<b>33</b>



# Introduction

## 1

*Positron emission tomography* (PET) is a medical imaging technique that uses small amounts of radioactive material to produce detailed images of biological processes inside the body. It is primarily used to diagnose diseases such as cancer, heart disease, and brain disorders as well as monitoring the effect of treatments [1, ch. 1]. The radioactive material, known as a radiotracer, is made by labeling a ligand (e.g. water, glucose, or various other molecules and hormones) with a radioactive isotope (e.g.  $^{15}\text{O}$ ,  $^{18}\text{F}$  and others). This radiotracer is injected into the patient's bloodstream, and after circulation, it will accumulate in certain parts of the body with a high affinity for this particular ligand. The ligand is thus chosen depending on the property that is to be measured. This could for instance be regions with high metabolism for the sugar analogous tracer *fluorodeoxyglucose* (FDG), where one of the oxygen atoms in the glucose molecule is replaced with the radioactive isotope  $^{18}\text{F}$ , which is widely used for detecting cancerous tumors as they have a high metabolic rate due to their rapid cell growth [2, 3].

The radioactive isotope used to label the tracer must be a positron ( $\beta^+$ ) emitter, as the scanner indirectly detects the presence and location of the radiotracer via the emitted positron. It does this from the fact that when a positron annihilates with an electron, two photons will be created. These are emitted  $(180.0 \pm 0.5)^\circ$  apart due to conservation of momentum and each photon have the equivalent energy of the rest mass of an electron, 511 keV. The small uncertainty in the angle between the emitted photons arises due to relative motion that may exist between the two particles before annihilation. If they annihilate at rest, the photons will be emitted back to back, however, in real situations, some unbalanced momentum will cause small deviations from being perfectly collinear. This fact plays a fundamental role in how accurately we can determine the actual position of the decayed isotope [1, ch. 2].

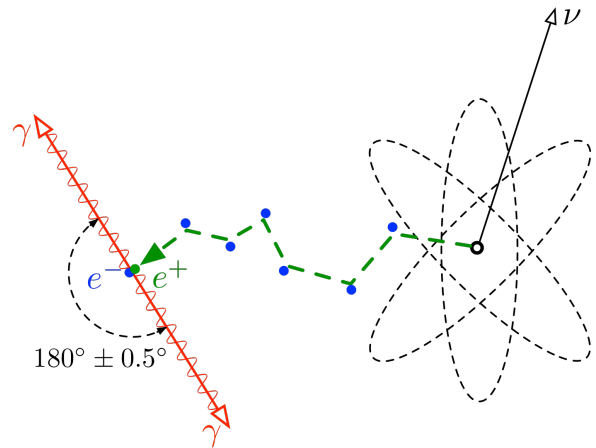


**Figure 1.1** – Schematic showing the process of isotope decay by positron emission, subsequent scattering and finally annihilation with an electron emitting two gamma quanta of 511 keV in opposite directions. (From Wikipedia.org ([https://en.wikipedia.org/wiki/Electron%E2%80%93positron\\_annihilation](https://en.wikipedia.org/wiki/Electron%E2%80%93positron_annihilation)).)

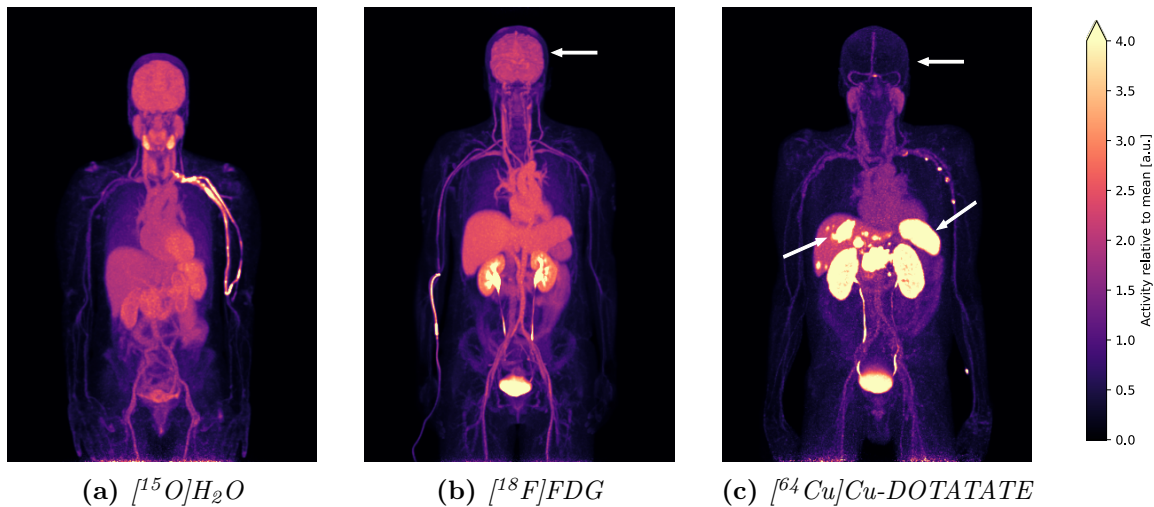


**Figure 1.2** – Coronal PET scans (maximum intensity projection) with three different tracers. Note the high activity in the brain for FDG due to its high metabolism in contrast to the low activity in the brain for DOTATATE as this tracer can not cross the blood-brain barrier [5, 6]. Also note for this tracer, the high activity in the spleen and the possible tumor in the liver (arrows) due to the high concentration of somatostatin receptors here in the spleen and in some types of tumors [7]. Water generally flows with the blood and diffuses easily through tissue, and thus shows blood flow and supply. The images are averaged from 1 min after tracer injection to 12, 60 and 45 min respectively. The scale shows the activity relative to the mean activity within each patient.

Because PET scanners detect the number of annihilation events at a given location within a patient, they are also used as a quantitative measurement device, as this number is directly related to the concentration of ligand at that location. This can then be used to e.g. determine the metabolic rate of tumors [4]. These are the general principles that PET scanners use to produce the detailed images that highlight the body's internal functions.

## 1.1 Tracers used in this project

There are several types of radiotracers that can be used in PET imaging [8], each with different properties and specific applications depending on what we wish to examine, but common for them all, as mentioned above, is that they must be  $\beta^+$ -emitter. We will refer to the *first-pass extraction fraction* of a tracer, which is a measure of how much of the tracer will be extracted from the blood vessels and absorbed into the surrounding tissue during its first pass [9]. It can be used to evaluate the function of organs by comparing the extraction fraction of an unhealthy organ with a healthy one, and depends on the type of tissue by which the tracer is passing, and therefore should be used in conjunction with other information if used for diagnosis [10].





Some commonly used radiotracers include the following, which are also the ones we will study and use in this report:

- **Fluorodeoxyglucose** ( $[^{18}\text{F}]\text{FDG}$ ) is a widely used radiotracer in the field of oncology to detect cancerous tumors with PET imaging [2] as it is analogous to and behaves similarly to natural glucose, but cannot be fully metabolized. This is due to the fact that FDG is labeled with the radioactive isotope  $^{18}\text{F}$ , hindering the final step of metabolism. This isotope decays via  $\beta^+$  and therefore makes it possible to detect and measure the cells' uptake of the tracer with PET. As cancer cells have a higher rate of glucose metabolism than other tissue, the tracer will naturally accumulate in these areas of increased glucose metabolism. It is produced
- **$^{15}\text{O}$ -labeled water** ( $[^{15}\text{O}]\text{H}_2\text{O}$  or  $\text{H}_2^{15}\text{O}$ ) is a non-invasive way of measuring blood flow and perfusion through organs as it is an easily diffusible molecule, which flows freely from blood to tissue [11, 12].  $[^{15}\text{O}]\text{H}_2\text{O}$  is particularly useful in the evaluation of the brain and heart, as well as in the evaluation of tumors [13, 14]. For example, it can be used to detect areas of decreased blood flow, which can indicate the presence of a blockage, for example a thrombosis or stenosis, or another problem in the blood vessels. Due to the very short half-life of  $^{15}\text{O}$  of around 2 min, it is necessary that the radiotracer is produced in a cyclotron on-site and used within a few minutes.
- **DOTATATE** ( $[^{64}\text{Cu}]\text{Cu}$ -DOTATATE) is a  $^{64}\text{Cu}$ -labeled somatostatin analogue that binds to somatostatin receptors. These receptors are found in the neuroendocrine system, but are over-expressed in neuroendocrine tumors and the radiotracer can accumulate here by binding to the somatostatin receptors on the tumor cells [7, 15]. The tracer is also not able to cross the blood-brain barrier [5, 6], which is also evident from the low activity in the brain in the PET scan for DOTATATE in Figure 1.2c.  $[^{64}\text{Cu}]\text{Cu}$ -DOTATATE has a half-life of 12.7 hours and as such remains usable for longer in the event that there is a delay along the way, and can easily be made in a specialized facility off-site to be delivered to the hospital [16].

The radioactive isotopes are produced by accelerating protons in a cyclotron up to energies of around 20 MeV and bombarding a target, after which it is chemically bound to a ligand. Each isotope has its own characteristics, such as half-life and emission energy, which can affect the image quality, resolution and the specific information that can be



**Table 1.1** – Properties of common  $\beta^+$ -emitting radiotracer isotopes (adapted from [17, Table 1]).

Isotope	Half-life	Mean $\beta^+$ energy (keV)	Mean $\beta^+$ range (mm)
$^{11}\text{C}$	20.4 min	386	1.2
$^{13}\text{N}$	10.0 min	492	1.8
$^{15}\text{O}$	2.0 min	735	3.0
$^{18}\text{F}$	110 min	250	0.6
$^{64}\text{Cu}$	12.7 h	278	0.7
$^{89}\text{Zr}$	3.27 d	396	1.3

obtained from a PET scan [17]. For example, an isotope with a higher emission energy will also cause the mean range of the emitted positron to increase, i.e. the positron will travel longer before annihilating with an electron from the tissue. This non-negligible distance between the location of the tracer, which is what we want to know, and the point of positron-electron annihilation, which is what we are measuring, results in a blurring around the tracer location, and a decrease in scan resolution, making it difficult to discern fine details and the precise distribution of the tracer [18]. Some properties of common tracer isotopes can be found in Table 1.1.

## 1.2 Using dynamic PET scans to study kinetics

A single PET scan produces a 3-dimensional image of the concentrations of radiotracer activity in units of Bq/mL (Becquerels per milliliter) for many small volumes within the body. These small volumes or *voxels* usually have a size on the order of a  $\text{mm}^3$ , and by capturing several scans one after another, we obtain a dynamic series of images and each of the voxels now has a so-called *time activity curve* (TAC) showing how the radiotracer concentration is evolving over time for the tissue enclosed in this voxel volume. See Figure 1.3 for examples of TACs: the input function derived from the aorta and a tissue voxel in the brain.

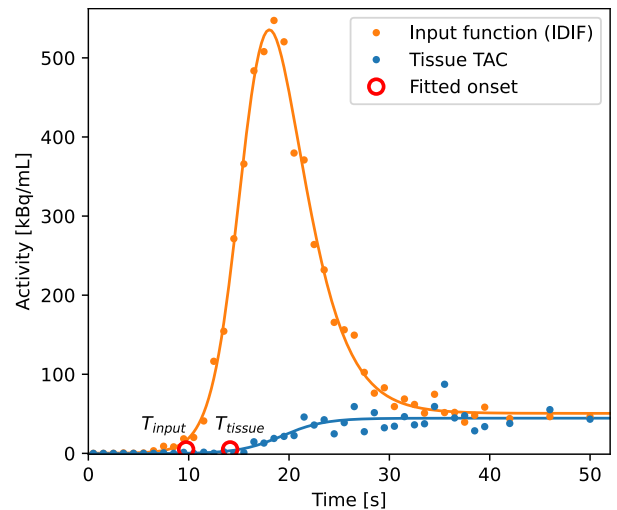


**Figure 1.3** – Example of two time activity curves (TACs): the input function (IDIF) and a tissue curve.

In this report we will be working with *dynamic* PET scans. These scans allow us to observe how the tracer flows through the body and to measure the rate at which specific

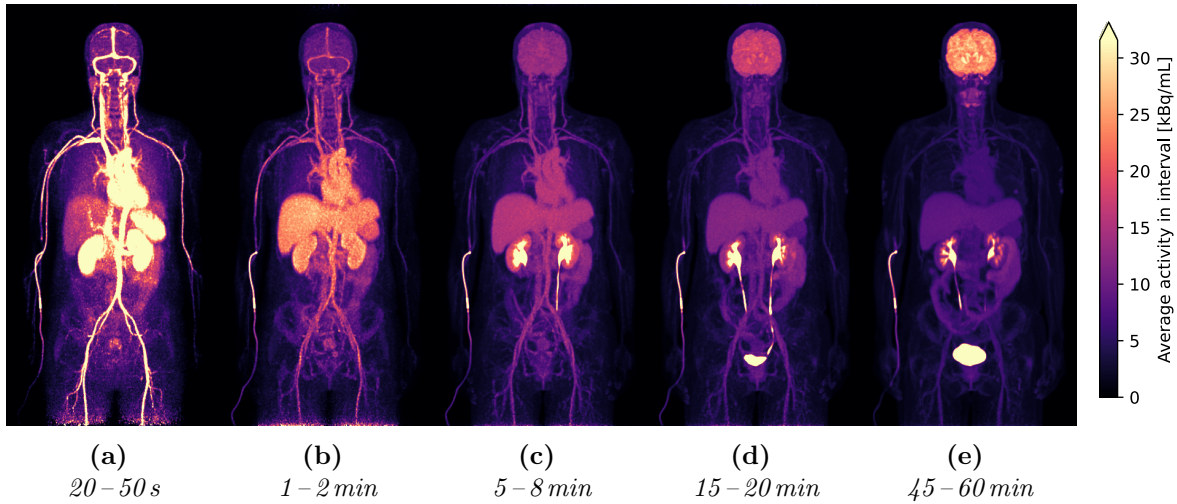


**Figure 1.4** – Coronal views of a dynamic  $[^{18}\text{F}]\text{FDG}$  PET scan (maximum intensity projection) for various intervals after injection of the radiotracer.

biological processes occur in the body, such as metabolism, blood flow or perfusion [4, 14]. The scanner captures a series of frames over the course of several minutes which can be used to determine these properties. Figure 1.4 shows a few frames from a dynamic PET scan for various intervals after injection of the radiotracer  $[^{18}\text{F}]\text{FDG}$ . The tracer quickly circulates through the body and the organs, but after the first few minutes some areas start to trap and accumulate the tracer. For FDG, this is usually the brain, bladder and tumors that are the most visible.

With quantitative kinetic PET analysis we wish to study how an organ of interest reacts to the injected radiotracer bolus over time using the dynamic scans, and model the resulting TACs to obtain parameters that can tell us about for example the blood flow among other properties. Ideally, the injection of radiotracer is to be administered as a quick and intense bolus in time, however, this is in practice not possible, and it is therefore necessary to know the actual shape of the input bolus in order to obtain useful quantitative measurements from the kinetic modeling [19]. We will go more into detail about this modeling in the Methods section.

The required input function can be acquired in a few different ways: by sampling blood directly from an arterial cannulation or by deriving it from the PET images are among the most popular techniques [20, sec. 5]. The former, the *arterial input function* (AIF), involves collecting blood samples from the patient at regular intervals after the radiotracer has been injected and measuring the radioactive concentration using a gamma counter. It is regarded as the gold standard for retrieving the input function, although it is rather invasive and time consuming [21]. The other method, the *image*



*derived input function* (IDIF), makes use of the dynamic PET scans themselves to derive the input function from a chosen volume of interest inside an artery. This method is on the other hand completely non-invasive, but depends on the quality of the segmentation, scan resolution and other effects such as partial-volume occurring between tissue and artery [22].

### 1.3 The advantage of long-axial field-of-view PET scanners

The most common size of PET scanners up till today have an axial field of view of around 25 cm – enough to cover a single organ [23]. This also means, e.g. in the case of brain studies, that it can be difficult to obtain a good quality IDIF from the carotid arteries. These are the largest arteries supplying the brain, but with an average diameter of around 5 mm [24] and PET resolution being around a few mm, they are too small to reliably segment and can cause partial volume effects where the signal from a voxel is shared by both the arterial blood and tissue [19]. However, if we instead acquire dynamic scans using a whole-body PET scanner, it enables us to use the aorta as a source for the IDIF instead, as it is a much larger artery, thus allowing for a better quality segmentation and hence a more accurate image derived input function.

Note in Figure 1.3 how there is a appreciable delay between the onsets of the two curves. This inherent delay between the input function and an organ, whether the input function is acquired by AIF or IDIF, is due to the fact that the input function is measured closer to the point of injection (hence also the name) than the tissue is and has to be corrected for before we can model it, such that the two curves line up in time. This is important because we wish to observe how the tissue reacts to the input we are supplying it with. The way delay correction is usually done [25, 26], is to average the TACs within the organ to be studied and find a mean delay for the whole organ, after which all the TACs are corrected by this mean delay – essentially moving all the TACs back by the same amount. This also means, however, in the case where there are regions in the organ with relatively large differences in delay, that some TACs can be severely under- or overcorrected, resulting in a biased kinetic analysis.

In addition to long-axial field-of-view scanner enabling multiple organs to be analyzed simultaneously, they also offer lower noise due to more lines of responses being permitted inside the scanner geometry [1], and thus more annihilation photons can be captured. This also allows for smaller doses to be administered to the patients [27] as well as better and low noise scans with high time resolution, which is crucial for kinetic modeling [28].



## 1.4 Aim of the project

In this report we wish to investigate and improve on kinetic flow analysis by developing a delay correction algorithm that can more closely match and correct for the local tissue delays relative to the input function at a single-voxel or near-single-voxel level. This will help to obtain more accurate and less biased results from kinetic analyses of organs with regional delays differing considerably from the mean organ delay. We will apply and evaluate this new delay correction method in kinetic modeling on two organs: the thyroid and the brain, with the use of dynamic PET scans from two groups of patients: patients with Graves' disease and patients with carotid stenosis, and observe the effect on blood flow in the organs after they receive a treatment or a drug.

Graves' disease is an autoimmune disorder that affects the thyroid and causes it to be overactive and over-perfused resulting in an overproduction of thyroid hormones, which control how different organs use energy [29]. The treatment of this disease involves giving the patient radioactive iodine-131 [29], which slowly kills the thyroid gland cells and thus the activity as well as the perfusion is expected to decrease as a result.

Stenosis in an artery makes it difficult for enough blood to be supplied to an organ or tissue, and hence there will also be a lower flow of blood to this organ or part of it, which can cause serious health effects and pain. Stenosis differs from a blood clot in that it is a narrowing of a blood vessel typically from a build-up on the inner walls of the blood vessels [30]. These patients will receive the drug acetazolamide, also known as, and referred to in this report as Diamox, which is known to increase blood flow in the brain by way of dilating the blood vessels [31], i.e. a vasodilate. The effect of Diamox on blood flow in different organs is, however, not yet fully documented, but with whole-body PET scanners we can test this more easily. In this report we will however focus only on the thyroid and brain to determine if this treatment of Graves' disease is local to thyroid or also affects the flow in the brain, and if the drug Diamox affects the flow in the thyroid in the same way as it does for the brain.

In the next chapter, we will cover the theory on how flow can be modeled, and later detailing the delay-finding algorithm.



# Theory

## 2

### 2.1 Compartmental modeling

One of the most common ways of modeling blood flow in an organ with PET is by using compartmental modeling [32]. This is a way to separate the states in which the tracer can be in, whether it is in the blood or the tissue or in a bound state within the tissue, and so on for more complex models. Each compartment can allow the tracer to flow to the other compartments and how easily the tracer does this is described by rate constants between each of the compartments. The radioactive concentrations in the compartments are labelled  $C_0$  through  $C_n$  with  $n$  being the number of tissue compartments, where  $C_0$  usually represents the radioactive concentration in the blood, while the other compartments describe the various states that the tracer can be in inside the tissue, with  $C_i$  being the radioactive concentration of the  $i$ 'th compartment. By convention, the rate constants are named  $K_1$  for flow from the (arterial) blood compartment ( $C_0$  or  $C_A$ ) to the first tissue compartment ( $C_1$  or  $C_T$ ); and  $k_2$  represents flow from the tissue back into the (venous) blood stream. If there are multiple tissue compartments, the additional unidirectional rate constants between these are named  $k_j$  as shown in Figure 2.1.

The simplest compartmental model is the *two-compartment model* – or equivalently the *one-tissue compartment model* (Figure 2.1a) – which has only two compartments in which the tracer can be suspended: arterial blood and tissue, with concentrations  $C_A$  and  $C_1$  and rate constants  $K_1$  and  $k_2$  between them. The rate constant  $K_1$  has units (mL blood)/(100 g tissue · min), i.e. the amount of blood that is flowing through 100 g of tissue per minute; and  $k_2$  (as well as the  $k_i$ 's for other higher order models) have units 1/min, representing the percentage of tracer that will flow to another compartment per minute.

We can describe the dynamics in this model with the differential equation

$$\frac{dC_1(t)}{dt} = K_1 C_A(t) - k_2 C_1(t). \quad (2.1)$$

The concentrations of the arterial blood compartment,  $C_A(t)$ , is the input function which has been derived from the PET images as described earlier, and  $C_1(t)$  is the tissue

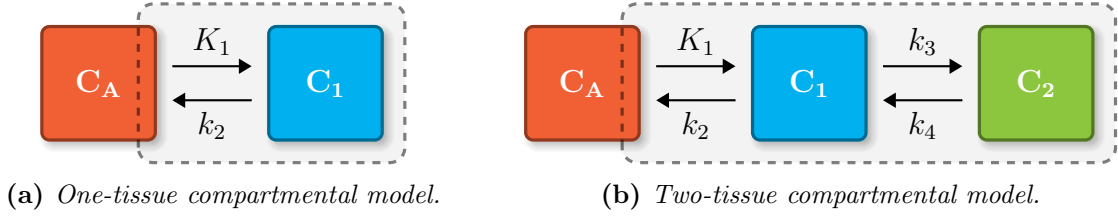


**Figure 2.1** – Schematics of different compartmental models (adapted from [33]).  $C_A$  is the tracer concentration in the blood compartment and  $C_1$  and  $C_2$  are the concentrations of either free or bound tracer in tissue.  $K_1$  and  $k_i$  are rate constants between each of the compartments, with  $K_1$  being the rate constant from blood to tissue.

TAC that we want to model. Because the tissue we are interested in might be placed at a different point in time in the circulatory system than the input function is, it will receive a delayed version of the input function, and we therefore need to correct the TAC for this delay in order to model the flow parameters correctly. To do this, we move the individual TACs back by their corresponding delay value found from the algorithm described above and interpolate them to the same time points as before.

By adding an extra tissue compartment to the model, we have the *two-tissue compartment model* (Figure 2.1b), which allows a tracer to be taken up by tissue and later enter a bound state. This bound state can be phosphorylation of glucose with the tracer [ $^{18}\text{F}$ ]FDG. The differential equations for the concentration dynamics in this model can be written as

$$\frac{dC_1(t)}{dt} = K_1 C_A(t) - (k_2 + k_3) C_1(t) + k_4 C_2(t), \quad (2.2)$$

$$\frac{dC_2(t)}{dt} = k_3 C_1(t) - k_4 C_2(t). \quad (2.3)$$

Quantification of perfusion or blood flow with freely diffusible tracers, such as [ $^{15}\text{O}$ ]H<sub>2</sub>O, is based on the one-tissue compartment model, while the two-tissue compartment model is for example used to model glucose uptake and phosphorylation using [ $^{18}\text{F}$ ]FDG [33].



# Methods



## 3.1 Setup

To summarize the goal and outline the groups and subgroups of patients we will be working with: we wish to determine the flow of blood through – or perfusion of – the thyroid in patients with Graves’ disease and to determine if there is a change in flow rates after the patients receive this treatment. To determine if the possible change in flow rates caused by the treatment is local to the thyroid, the blood flow in the brain of these patients will also be modelled. In short, Graves’ disease is causing the thyroid to be overactive and the blood flow through it will similarly be increased.

A healthy control group will be used to compare the patients before and after treatment. Although the number of patients in the control group is limited, we can also to some degree use data from patients who had scans done for other reasons. It is, however, important to note that these other patients are not necessarily healthy, but are diagnosed with carotid stenosis that might affect the results, but by making sure to include as many of them as possible, we may be able to obtain a representative distribution of flow rates in the thyroid for patients without Graves’ disease.

This other group of patients, diagnosed with carotid stenosis, had scans done with and without the drug Diamox. This drug helps to dilate the blood vessels and hence increase the flow of blood. It is known to affect the flow in the brain [31], but the effect on blood flow in other organs is not yet fully known. We will therefore also model both the brain and thyroid for these patients to estimate the blood flow rates and to determine if there is a change in flow in the organs upon receiving the drug.

We now have two groups of patients: patients related to Graves’ disease and patients related to the drug Diamox; each of them with subgroups: before and after treatment for the Graves patients as well

**Table 3.1** – Overview of patient groups. The blood flow will be modelled for both the thyroid and brain for each subgroup.

	Thyroid flow	Brain flow
<b>Graves</b>		
• Before treatment	-	-
• After treatment	-	-
• Healthy control (HC)	-	-
<b>Diamox</b>		
• At rest	-	-
• With Diamox	-	-





as the control group, and the other group at rest and with Diamox. All patients were scanned with the radiotracer  $[^{15}\text{O}]\text{H}_2\text{O}$ , which, due to its high diffusibility, makes it a popular choice for estimating blood flow [34]. Refer to Table 3.1 for an overview of the patient groups involved. In the results section, figures comparing these groups will use the corresponding colors for consistency.

We will start by detailing the delay-finding algorithm and the reason for each part, and later detail how we will apply it for flow modeling. But first and foremost, how the data was acquired and the tools that are used.

## 3.2 Data acquisition

Patients were scanned in a long-axial field of view PET/CT scanner (Siemens Biograph Vision Quadra [35]) immediately after injection of the radiotracer as well as a complimentary CT scan used for attenuation correction and organ segmentation. The tracers used are the three tracers introduced in the previous section:  $[^{15}\text{O}]\text{H}_2\text{O}$ ,  $[^{18}\text{F}]\text{FDG}$  and  $[^{64}\text{Cu}]\text{Cu-DOTATATE}$ . Due to their different half-lives, the total durations of the scans were different for each of the tracers as well as the number of frames captured in this time. Each frame or still-image is made up of a number of planes or slices in the axial direction, and these are stacked to create a 3-dimensional scan.

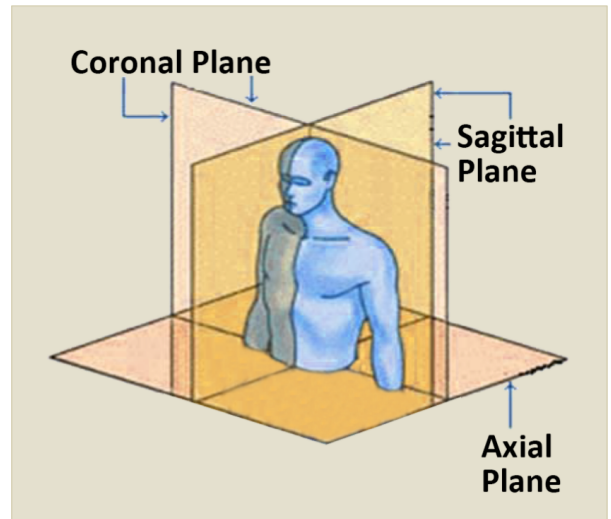


**Figure 3.1** – Schematic showing how the body is divided into coronal, sagittal and axial planes. (From IPF Radiology Rounds (<https://www.ipfradiologyrounds.com/hrct-primer/image-reconstruction/>).

For  $[^{15}\text{O}]\text{H}_2\text{O}$  the number of axial slices were 645 and for FDG and DOTATATE it was 531. Since the field of view is the same for all the scans, as they were captured using the same scanner, the voxels' axial length varies slightly between the tracers, with the  $[^{15}\text{O}]\text{H}_2\text{O}$  scans having voxel dimensions (coronal, sagittal, axial – see Figure 3.1 for visual definitions) of  $1.65 \times 1.65 \times 1.65 \text{ mm}^3$  and the FDG and DOTATATE scans having voxel dimensions of  $1.65 \times 1.65 \times 2 \text{ mm}^3$ . This gives us a 72.6 cm view in the coronal and sagittal directions and an axial coverage of 106 cm for all the scans, allowing us to view all the vital organs in the same frame.



From 0–40 s after tracer injection, the frame duration or integration time of each frame was 1 s/frame. This covers the bolus onset as well as the peak of the TAC bolus. After 40 s from the injection, the frame duration was increased to 4 s/frame and later to 10 s/frame. Refer to Table 3.2 for a summary and overview of the details of the scans of each of the three tracers.

To make sure the PET scans are reliable, each patient was scanned twice per session, which will allow us to test the reproducibility between the two scans and hence quickly determine if something is wrong with either of the scans if they deviate too much. In total, scans from 22 patients are tested, and out of these, 5 had Graves’ disease, 3 of which also received treatment for it and 5 are healthy controls; and in the other group, 12 patients received the drug Diamox and had scans at rest and with the drug. In the development of the delay finding algorithm, additional patients were used for testing and to improve it. These include 5 patients who received [<sup>18</sup>F]FDG and 5 patients who received [<sup>64</sup>Cu]Cu-DOTATATE, giving us a large interval of extraction fractions over which to test and improve the algorithm.

All processing of data is coded using Python version 3.6.8 with Numpy v. 1.19.5 and Scipy v. 1.5.4 for data handling. Matplotlib v. 3.3.4 is used to produce the plots, in addition to various other modules used to load data, parallelize computations and for debugging. For flow modeling, the scripts `imgflow` [36] and `fit_h2o` [37] v. 0.7.9 written in C and developed by Turku PET Centre [38] are used.

**Table 3.2** – Scan details across the three tracers.

Tracer	[ <sup>15</sup> O]H <sub>2</sub> O	[ <sup>18</sup> F]FDG	[ <sup>64</sup> Cu]Cu-DOTATATE
Isotope half-life	2 min	110 min	12.7 h
Scan time	12 min	60 min	45 min
No. of frames captured	64	87	84
No. of axial slices	645	531	531
Voxel dim. (cor, sag, ax) [mm]	1.65, 1.65, 1.65	1.65, 1.65, 2	1.65, 1.65, 2
Scan dim. (cor, sag, ax) [cm]	72.6, 72.6, 106	72.6, 72.6, 106	72.6, 72.6, 106



### 3.3 Delay map algorithm

We are interested in determining the difference in onset times between a tissue TAC and the input function,  $\Delta T = T_{tissue} - T_{input}$ , as this will later be used to correct for the delayed response of the tissue to the given input.

The input function is derived from averaging a volume inside the aorta from the PET images themselves (see the red area in Figure 3.2), because this is a large artery that does not move significantly between frames as opposed to the inside of the heart or a smaller artery. This is the *image derived input function* (IDIF) and the volume is found using a machine learning algorithm analogous to an organ segmentation method we will introduce later on page 19.



**Figure 3.2** – Example CT scan of the location in red inside the aorta from where the IDIF is derived.

#### Fitting the time activity curve

An example of a tissue TAC and an input function (IDIF) is plotted in Figure 3.3a. We observe for both the curves that they start with an activity of 0 and around the onset times  $T_{input}$  and  $T_{tissue}$ , each curve starts to increase. The tissue TAC increases to a saturation level and can be fitted well by this equation found empirically:

$$A_{tissue}(t) = \frac{a}{1 + \exp\left(\frac{c-t}{b}\right)}, \quad (3.1)$$

where  $a$  is the amplitude or saturation level when  $t$  is large, i.e.  $t \gg c$ ;  $b$  tells how rapid the function transitions from 0 to the saturation level,  $a$ , where  $b = 0$  means the change happens instantly; and  $c$  is the center point around which the function transitions.

The input function, being taken from an artery, is slightly different as it increases rapidly after which it drops down to a steady-state level, due to the fact that an artery transports fluid and that there is no tissue inside in which the tracer can be absorbed into apart from the blood and plasma. Empirically, the input function, or any other arterial time activity curve can be fitted with a slightly more involved but similar function that

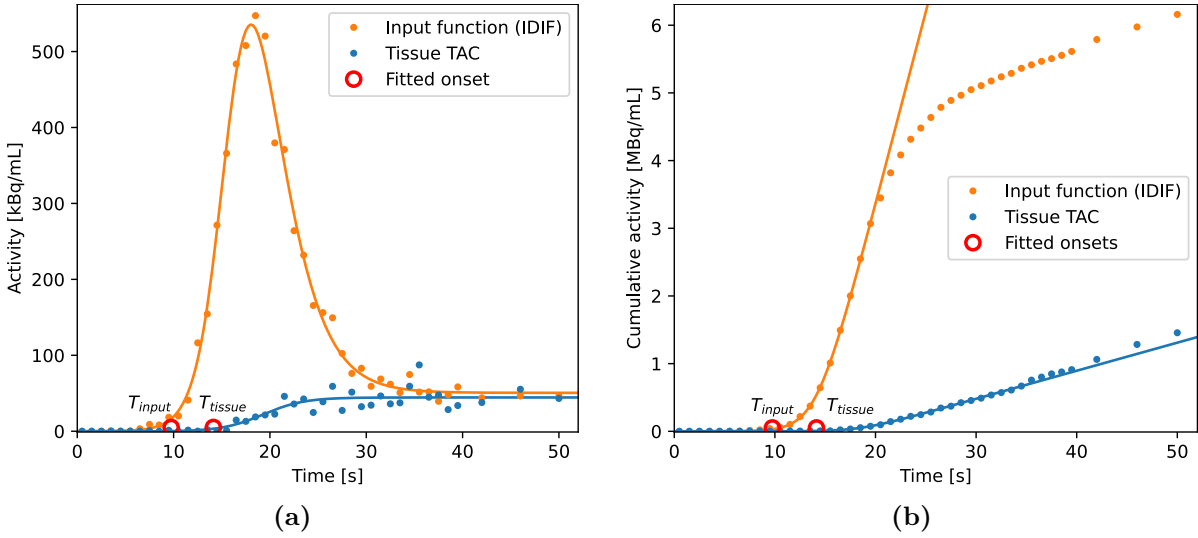


**Figure 3.3** – (a) shows typical time activity curves (TACs) for a single voxel tissue TAC and the input function (IDIF), and (b) shows the cumulative sum of the same data. Note how the tissue TAC increases due to absorption while the input function, being a blood TAC, shows a large increase in tracer concentration before decreasing to equilibrium. Also note how the signal-to-noise ratio is significantly improved in (b) after being summed cumulatively, making it easier to obtain a good fit.

is a sum of three  $A_{tissue}$ :

$$A_{artery}(t) = \frac{a_1}{1 + \exp\left(\frac{c_1-t}{b_1}\right)} + \frac{a_2}{1 + \exp\left(-\frac{c_2-t}{b_2}\right)} + \frac{a_3}{1 + \exp\left(\frac{c_3-t}{b_3}\right)}, \quad (3.2)$$

where the two first terms describe the exponential increase and decrease of the activity (note the negative sign in the exponential of the latter), while the last term describes the steady-state level. Each  $a$ ,  $b$  and  $c$  describe the amplitudes of each term, how rapid they transition and when they make this transition, respectively.

In principle, it is also possible to fit the tissue TACs with  $A_{artery}(t)$ , however, it will be too complicated as most of the tissue TACs do not exhibit the same shape as the arterial TACs do, and hence we may obtain inaccurate or misleading fitting parameters. On the other hand, all TACs exhibit the same up-slope around the transition from zero activity to the peak or saturation level. We will therefore focus on fitting the up-slope instead of the full TAC in order to determine the onset time.

Most single voxel TACs have a very small signal-to-noise ratios, which is also evident in Figure 3.4, where, as we approach a single voxel, fitting the data with Equation 3.1 becomes rather difficult. However, as the noise is approximately Gaussian distributed, summing the data cumulatively will cancel out most of the noise and we obtain a nearly straight line which improves the fitting quality significantly. The new fitting equation is

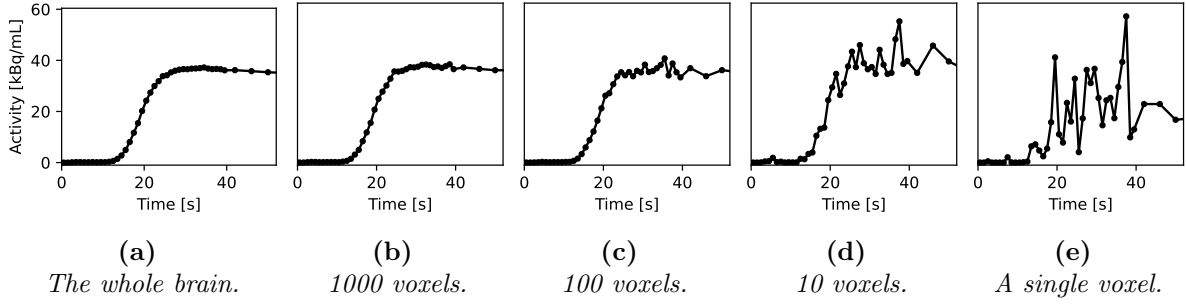


**Figure 3.4** – The time activity curves (TACs) obtained by averaging a number of voxels within the brain to visualize the shape of a tissue TAC and how the signal-to-noise ratio changes with smaller volumes. Here is shown from left to right the TACs obtained from averaging 20 million voxels (the whole brain), 1000, 100 and 10 voxels and at last a single voxel. It is important to note, however, that even single voxel TACs can look very different from each other.

then the integral of  $A_{tissue}(t)$  (Equation 3.1) from 0 to  $t$ :

$$A_{sum}(t) = \int_0^t A_{tissue}(t') dt' = ab \ln \left[ \exp\left(\frac{c-t}{b}\right) + 1 \right] + a(t-c), \quad (3.3)$$

with the same parameters as before:  $a$  is the amplitude and  $b$  is how quickly the function transitions around the point  $c$ .

### Choosing the best fit

The resulting summed input function and tissue TAC is plotted in Figure 3.3b with their fits using Equation 3.3. One thing to note is that especially arterial TACs (or more generally blood TACs) will have a noticeable fall-off in the summed view, and as the fitting equation tends to the asymptote  $A_{sum}(t \gg c) \rightarrow a(t-c)$ , we must choose a range to fit that stops just before it falls off. Calculating the second order derivative of the TAC will reveal points where the curve “accelerates” up as the bolus arrives and later a “deceleration” to equilibrium. The points with a negative second derivative is where the summed TAC will show a tendency to fall off. Here we choose 10 different ranges of the data to fit and we can find the one that produces the best fit. The endpoints of the 10 data ranges are chosen by the most negative second derivative first as this will have the highest chance of being the best fit. The fit quality is determined from the  $R^2$ , defined as

$$R^2 = 1 - \frac{\sum_i (y_i - f_i)^2}{\sum_i (y_i - \bar{y})^2}, \quad (3.4)$$

where  $y_i$  is the  $i$ 'th observed data point with  $\bar{y}$  representing the mean and  $f_i$  being the value predicted by the fit. Here we extend the fitted data range with 3 extra data points



in the calculation of the  $R^2$  to filter out fits that blow up due to sudden large noise spikes and other types of noise in the data and instead favor fits where the summed TAC separates from the fit relatively slowly.

The onset time,  $T$ , can then directly be estimated using the optimal parameters from the fit with the highest  $R^2$ , and the best combination of fitting parameters was found empirically to be  $T = c - \frac{5}{2}b$ . The parameter  $c$  determines the central position of the curve, but as  $b$  (the tightness of the curve) changes from small (quick transition) to large (slow transition), we need to correct for the fact that the onset time,  $T$ , lies earlier than the center of the curve transition,  $c$ .

Bounds for the fit parameters are set to  $a \in [0.1, 2 \times 10^7]$ Bq/s,  $b \in [0.01, 10]$ s,  $c \in [0, 60]$ s, and as a rough constraint for the calculated onset time,  $T$ , it should be within a range from when the first signal is detected to the peak of the TAC. To increase the chance of a good fit for TACs with an onset time close to the beginning of the data set (e.g. the parts close to the area of injection), a number of zeros are prepended to the data before running the fitting algorithm.

### Addressing other sources of noise

Some TACs will exhibit random noise spikes in the early part, and the fit might confuse these with the actual onset time. To mitigate this, we run a plateau finding algorithm on the cumulatively summed data to find places of 4 or more data points that lie within a band of 1% of the peak value of the TAC. This percentage is chosen relative to the TAC being fitted instead of a fixed value such that it accommodates both high and low activity TACs.

In the time frame of a single scan, the patient will unavoidably move. This could for instance be breathing or the heart pumping, as well as other small uncontrollable movements. This could affect the data as the tissue from one voxel would shift into a neighboring voxel, interfering with the signal and possibly causing noise in some cases. We can average a cube of the nearest neighbors around a voxel to help smoothen the data based on the surrounding tissue. This will help increase the chance of a better fit for TACs where it is not possible to fit the data well due to too much noise. After the first run of the algorithm with no nearest neighbor averaging, TACs with an  $R^2$  below 0.1 are averaged with their nearest neighbors in a cube of 5-by-5-by-5 voxels, and the delay-finding algorithm is run again on these TACs only. This helps achieve better fits and thus more accurate onset times in these edge cases for around 90% of the TACs



that had a too low quality fit.

The parameters that have been presented here can be tweaked manually to amplify or diminish the sensitivity and response of the specific part of the algorithm they control. Given the large variation in the extraction fractions of different types of tracers, in addition to many other physiological properties that may affect the signal and shape of the TACs, there may be cases where the optimal parameters may vary slightly from the ones presented here. In this report, we will however use the same values throughout, as described above.

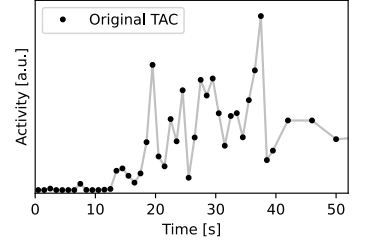
In summary, the delay-finding algorithm employs several techniques to overcome the different types of noise in the data. In short, it works by the following steps, which are also plotted in the figures on the right for a better visual understanding.

1. Summing the original TAC cumulatively to increase the chance of a successful fit (Figure 3.5b),
2. Calculating the second derivative and choosing 10 ranges to fit based on the most negative values (Figure 3.5c),
3. Finding the best of all the 10 fits from the one with the largest  $R^2$  (Figure 3.5d),
4. Calculating the onset time from the fitting parameters:  

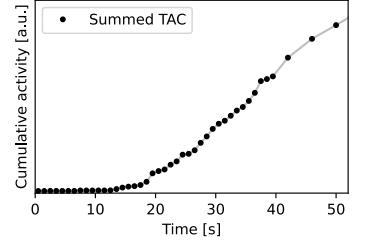
$$T = c - \frac{5}{2}b$$
 (Figure 3.5e).

If all the fits for a voxel end up having an  $R^2$  less than 0.1, the nearest neighboring voxels are averaged and the algorithm is run again on this voxel.

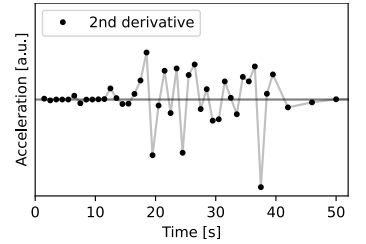
Finally, the onset time that is found for the TAC is subtracted by the IDIF onset time, found in the same way. Repeating these steps for each voxel, we can obtain an image of the delay times in a patient. This will be presented in the Results section.



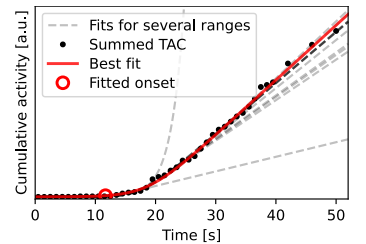
(a) *Original TAC.*



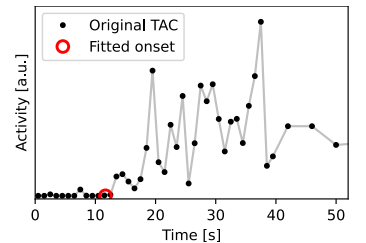
(b) *Cumulatively summed TAC.*



(c) *2<sup>nd</sup> deriv. of (b). Neg. values indicate ranges to fit.*



(d) *Best fit among 10.*



(e) *Original TAC with fitted onset.*

**Figure 3.5** – Steps in delay-finding algorithm.



### 3.4 Modeling flow using compartmental modeling

From dynamic PET scans with a long axial field of view it is possible to model multiple organs in the same patient simultaneously. Flow modeling can be done with compartmental modeling as described in Section 2.1 with a one-tissue compartment model using the patients who were scanned with  $[^{15}\text{O}]\text{H}_2\text{O}$  as the tracer, due to its high extraction fraction.

To model the flow in the brain and thyroid, we will be using a script developed by Turku PET Centre: `imgflow` (version 0.7.9) [36], which employs a one-tissue compartment model to fit the delay corrected time activity curves with. We will obtain distributions, or flow maps, over the flow rate parameters  $K_1$  and  $k_2$ , where for an extraction fraction assumed to be equal to 1 as for  $[^{15}\text{O}]\text{H}_2\text{O}$ ,  $K_1$  will equal the blood flow. The options given to the script are `-density`, which assumes a tissue density of 1.04 g/mL such that we obtain values with unit in terms of per 100 g tissue; `-mL` to obtain values with units in terms of mL blood as opposed to the default being mL blood; and at last, `-noneg` to run the model with strictly positive values for  $K_1$ .

The distribution we obtain of the flow for an organ is averaged before being compared with the other patients. This allows us to visualize and get an overview of how the parameters change as we go from one subgroup of patients to another (e.g. before treatment to after treatment).

### 3.5 Comparing the resulting flow between the two delay correction methods

As mentioned in the Introduction, the conventional way of correcting for the delay is done by averaging all the TACs within an organ or interest, such that you obtain a single TAC for the whole organ, much like in Figure 3.4a. Then find the delay between this organ mean TAC and the input function and move all the TACs in the PET scan back by the same amount. The new delay correction method consists of, as described earlier, by finding the delay for each voxel and moving them separately by their individual delay.

In order to assess the new delay correction method, we will compare the resulting flow found by the conventional method and by the new method. Two copies of a PET scan will be prepared, delay corrected with one of the methods each. They will both





have their flow modeled using the technique described above in Section 3.4, and finally the difference is visualized by subtracting the two flow maps from each other.

As discussed, carotid stenosis causes a greater difference in blood flow and delay between the two hemispheres of the brain. From the resulting delay maps of the patients with this diagnosis, we find a patient with a large variation in delay between the left and right hemispheres to compare the difference in flow we obtain from the two methods:  $\Delta K_1 = K_1^{new} - K_1^{conv}$ .

### 3.6 Organ segmentation

A whole-body PET scan also contains a lot of air around the patient with no usable information. To restrict the algorithm to only the area of the scan where the patient is, we use a mask derived from an accompanying CT scan. The mask is produced by a machine learning based organ segmentation algorithm called “MOOSE” [39], which recognizes and labels organs and the types of tissue within a patient based on the CT scan (see Figure 3.6). The space in which the CT and PET scans are in differ due to how they each capture their scans. This “space” holds information about the positions of the voxels in the real world, and to be able to match a CT scan to a PET scan, it is necessary to first transform it from its own space to the other. As mentioned, MOOSE masks are created from CT scans and must therefore be transformed into PET space and interpolated to match the same resolution. After this, it is then possible to restrict the algorithm to the voxels that lie within the edge of the patient or even single organs to study how the delay times as well as other parameters are distributed.

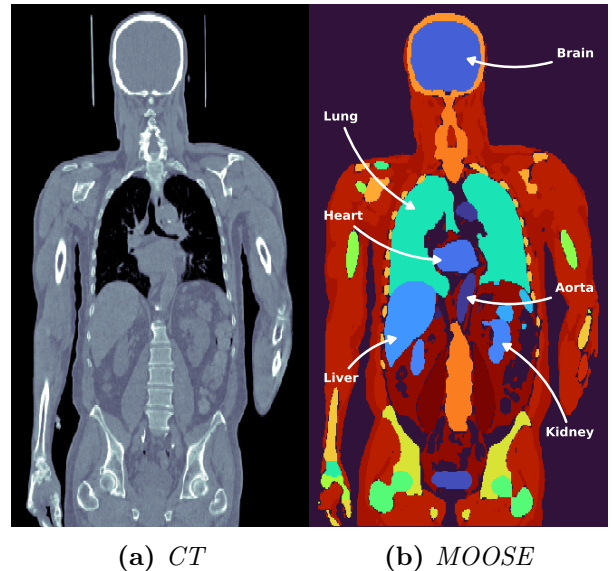


**Figure 3.6** – CT-scan (left) of a patient taken in conjunction with a PET scan for reference and to be used for organ segmentation (right), which is done here using MOOSE [39]. Each organ is given a unique number which can later be used to mask it out in the PET scan.



# Results

## 4

### 4.1 Delay map

By fitting every TAC in the patient and finding the delay between these and the input function, we can produce a map of the tracer delays which allows us to observe how the tracer is transported with the blood through the body to the different tissues. Examples of delay maps are shown in Figure 4.1 for three different patients receiving a different tracer each. The images exhibit some form of noise as is expected from the fact that single voxels inherently do contain noise, especially for tissue with low blood flow, and hence low signal in the PET images. However, we can still observe how the blood flows through the body from blue to red in the figures: first from the arm in which the injection took place to the right atrium and ventricle, next to the lungs and then to the left atrium and ventricle after which it enters the aorta and is pumped out to the rest of the organs and tissue. It is possible to discern the large arteries that supply the lower torso as well as the legs.

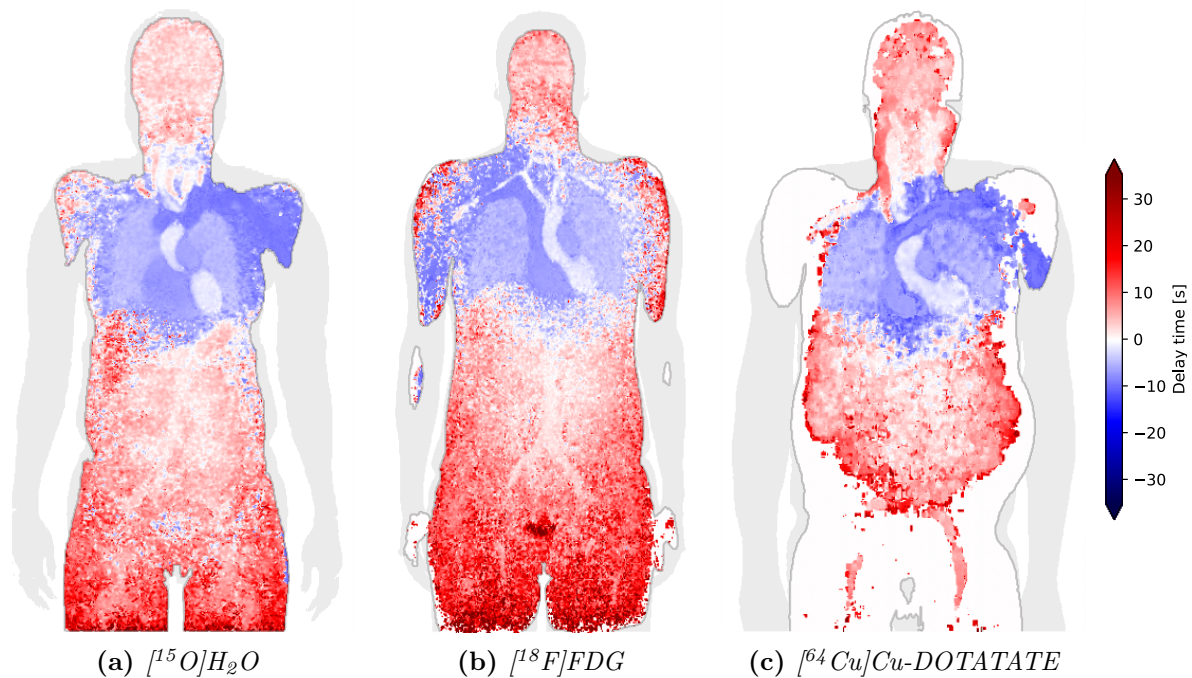


**Figure 4.1** – Examples of delay maps, here seen for a single plane, for three patients at rest, each receiving a different tracer with extraction fractions of around 1, 0.2 and  $\sim 0$  respectively [40, 41, 42]. The gray shadow represents the patient's projection, to serve as a guide, and the line outlines the plane in focus. White areas in the delay map are where the algorithm could not estimate the delay time.

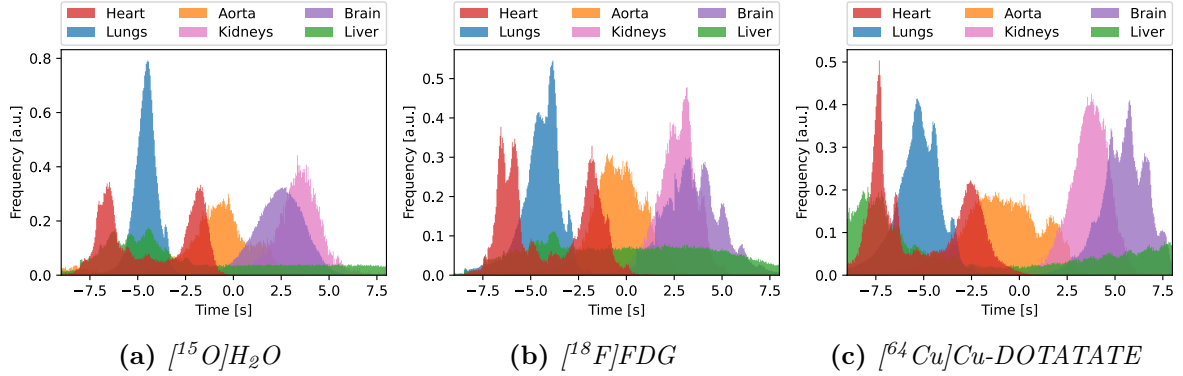


**Figure 4.2** – Example delay distributions in selected organs for three patients receiving one of the three tracers. Each organ histogram has been normalized. The histograms are plotted with 400 bins in the range  $(-9\text{ s}, 8\text{ s})$ , resulting in a bin size of approx. 43 ms.

The values given to each voxel in the delay maps mark the first point in time where the appearance of tracer is observed, and thus second pass as well as other subsequent passes are not registered. Each of the tracers used in Figure 4.1 have different extraction fractions, which affect the signal-to-noise ratio of the individual TACs and thus the ability for the algorithm to correctly recognize the actual tracer appearance times. This is especially evident in the delay map for  $[^{64}\text{Cu}]\text{Cu-DOTATATE}$  where there is not enough signal in the legs of the patient and only the iliac and femoral arteries, being the largest arteries in the upper legs, show up.

With the CT derived masks made using MOOSE [39], we can isolate organs and study the distribution of delay times in each of them. A histogram of the delay distributions of selected organs is plotted in Figure 4.2 and the mean delay times for the same organs are listed in Table 4.1. In the histograms we can observe two peaks for the heart, being the right and left ventricle, with the lungs receiving the tracer between these two peaks of the heart. We also observe that this is then followed by the aorta, and next the remaining organs receive the tracer after a period of time depending on their supply of blood and distance from the heart consistent with the delay maps. The liver receives both arterial and venous blood [43], which makes it span a broader interval until the whole organ has received the tracer. This can also be observed in the delay maps where the liver is colored

**Table 4.1** – Mean delay times and standard deviations obtained from the delay maps for three different patients – one for each of the tracers.

Organ	Mean delay [s]		
	Water	FDG	DOTATATE
Heart	$-4 \pm 2$	$-4 \pm 2$	$-5 \pm 2$
Lungs	$-4.6 \pm 0.7$	$-4.5 \pm 1.2$	$-5 \pm 2$
Aorta	$-1 \pm 2$	$-0.6 \pm 1.7$	$-2 \pm 3$
Kidneys	$3.4 \pm 1.4$	$2.6 \pm 1.2$	$3.7 \pm 1.1$
Brain	$2.4 \pm 1.3$	$3.5 \pm 1.8$	$6 \pm 2$
Liver	$0 \pm 7$	$0 \pm 5$	$4 \pm 11$

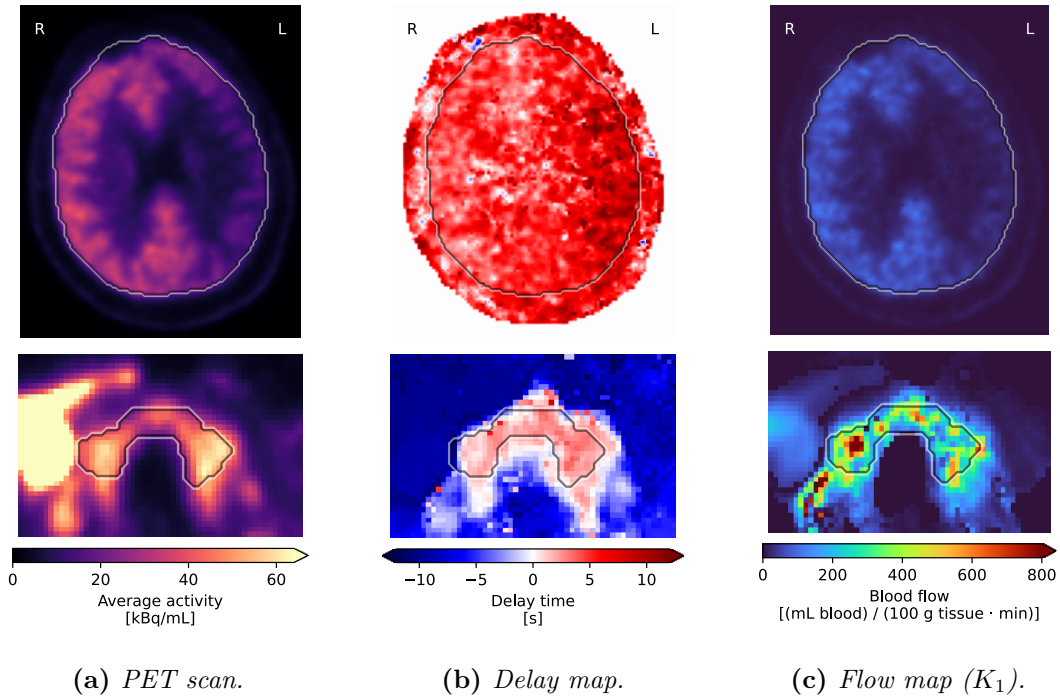


**Figure 4.3** – From a set of dynamic PET scans (a), we obtain a map of the tracer appearance times (b). Using this to delay correct the PET TACs, we can model the flow and obtain a map of the blood flow (c). In these figures are shown an example of the brain of a patient with stenosis in the left carotid artery (hence less tracer activity, higher delay and lower blood flow in this region) receiving Diamox, and the thyroid of a patient with Graves’ disease (note the parts with extreme flow). The outlines mark the boundary of the organ masks. Each set of images has been normalized to increase the contrast within the organs while still allowing for comparison between the two.

both blue and red. Each organ’s histogram has been normalized to increase the visibility of each of them and to show the proportion of the organ receiving the tracer at a given point in time.

## 4.2 Comparison of delay correction methods

### Modeling flow

From a series of PET scans (an average of which is shown in Figure 4.3a for the brain and thyroid), we have obtained delay maps of the two organs, as can be seen in Figure 4.3b. These maps are used to correct each individual PET TAC for their respective delay before modeling the blood flow, which is shown for both organs in Figure 4.3c. Note that the images of the brain and the thyroid in these figures are for a patient with stenosis on their left side receiving Diamox, and a patient with Graves’ disease prior to receiving treatment, respectively.

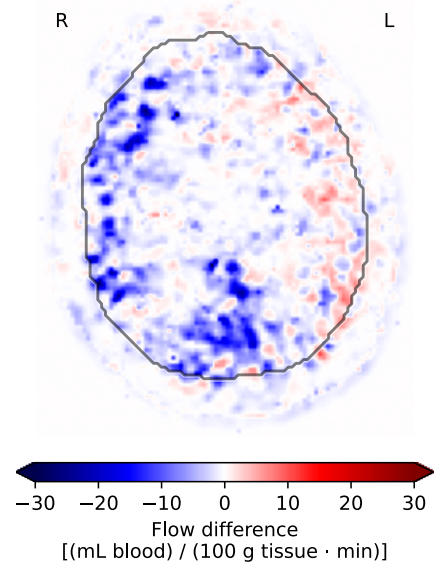


The conventional method of correcting the PET TACs for tracer delay is to move all the TACs in an organ by the same delay found from the average organ TAC [25]. This method does not take into account the regional differences there may be due to for example the size of the organ or problems for the blood to reach certain parts such as a stenosis or thrombosis.

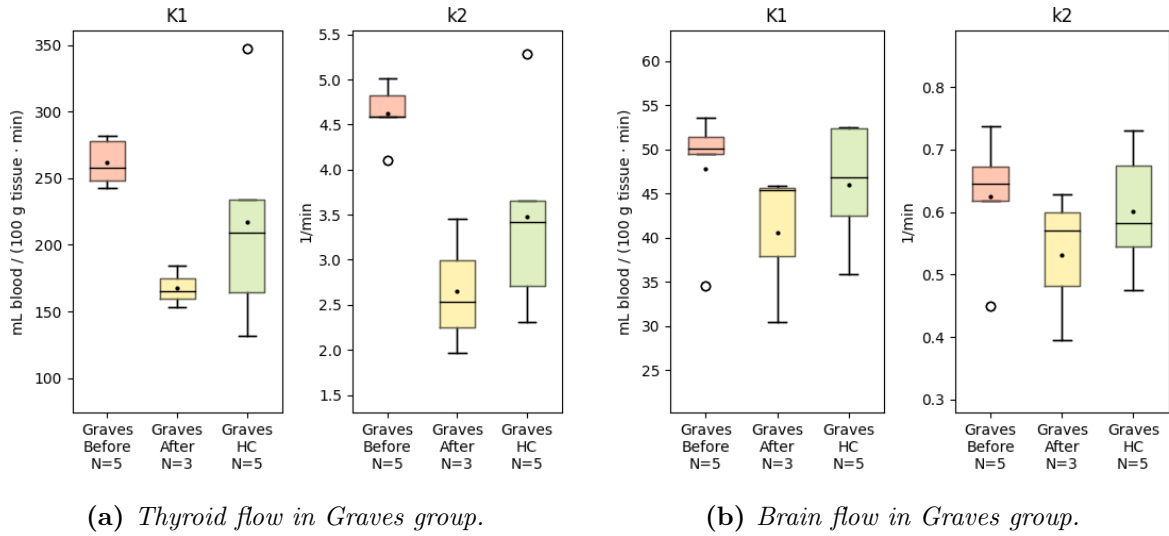
The patients in the “at rest/Diamox” group are patients who have been diagnosed with carotid stenosis, causing less flow to some regions in one of the hemispheres in the brain. We can use this to evaluate the improvement gained by the new single-voxel delay correction over using the conventional mean-organ delay correction method. A scan from one of the patients in this group who has a severe case of carotid stenosis is used, as it leads to larger differences in blood flow between the two hemispheres of the brain, and we thus expect to observe the largest discrepancy between these two methods here.

Figure 4.4 shows the absolute differences in modelled blood flow between the two methods mentioned,  $\Delta K_1 = K_1^{new} - K_1^{conv}$ , in an axial slice in the brain of a patient receiving Diamox with severe carotid stenosis on their left side. The change of using the new method to correct for delay can here directly be observed with estimated blood flow rates being biased towards more extreme values for the conventional method, with  $K_1^{conv}$  estimating larger flow rates than  $K_1^{new}$  in the high-flow regions (patient’s right side), and lower flow rates in the low-flow regions (patient’s left side).

Additionally, the differences in estimated flow rates between the two methods can be observed to have regional differences of up to around  $\Delta K_1 \sim 30 \text{ mL}/(100 \text{ g} \cdot \text{min})$ , which is about on the order of the mean flow rate in the brain for patients receiving Diamox (as per the results on the next pages, Figure 4.6b and Table 4.2) of  $\overline{K_1^{brain}} \approx 50 \text{ mL}/(100 \text{ g} \cdot \text{min})$ .



**Figure 4.4** – Differences in modelled flow using single-voxel delay correction and conventional organ-mean delay correction from Turku [38],  $\Delta K_1 = K_1^{new} - K_1^{conv}$ . The patient has stenosis on their left side.



**Figure 4.5** – Box plot comparison of the distribution of the mean flow parameters  $K_1$  and  $k_2$  in the thyroid and brain between patients with Graves’ disease before and after treatment as well as a healthy control group (HC). The black line and the black dot show the median and mean.  $N$  is the number of patients in each subgroup.

### 4.3 Results from flow modeling

Finally we wish to apply the new delay correction method to patients whose flow we can model before and after receiving treatment or drug to observe the difference and if it aligns with expectations.

The mean value of the flow parameters  $K_1$  and  $k_2$  for the thyroid and the brain of each subgroup of patients are listed in Table 4.2.

Figure 4.5 collects the mean flow parameters,  $K_1$  and  $k_2$ , in patients with Graves’ disease before treatment, after treatment and for the healthy control group. In total scans from 5 patients with Graves’ disease have been analyzed, 3 of which also had scans done after receiving the treatment, and 5 patients in the healthy control group.

A noticeable drop in  $K_1$  and  $k_2$  for the thyroid can be observed in patients after receiving the treatment, with a decrease of  $-35\%$  for  $K_1$  and  $-42\%$  for  $k_2$ . The untreated patients have flow parameters that lie above the mean of the healthy controls (abbreviated HC in the figure) with a difference of  $+20\%$  for  $K_1$  and  $+33\%$  for  $k_2$ , while the treated patients have flow parameters that lie below the mean of the healthy controls with a difference of  $-23\%$  for  $K_1$  and  $-24\%$  for  $k_2$ .

A T-test can help reveal how likely it is for two different distributions to come from the same distribution, where small p-values less than around  $1\%$  indicate a significant

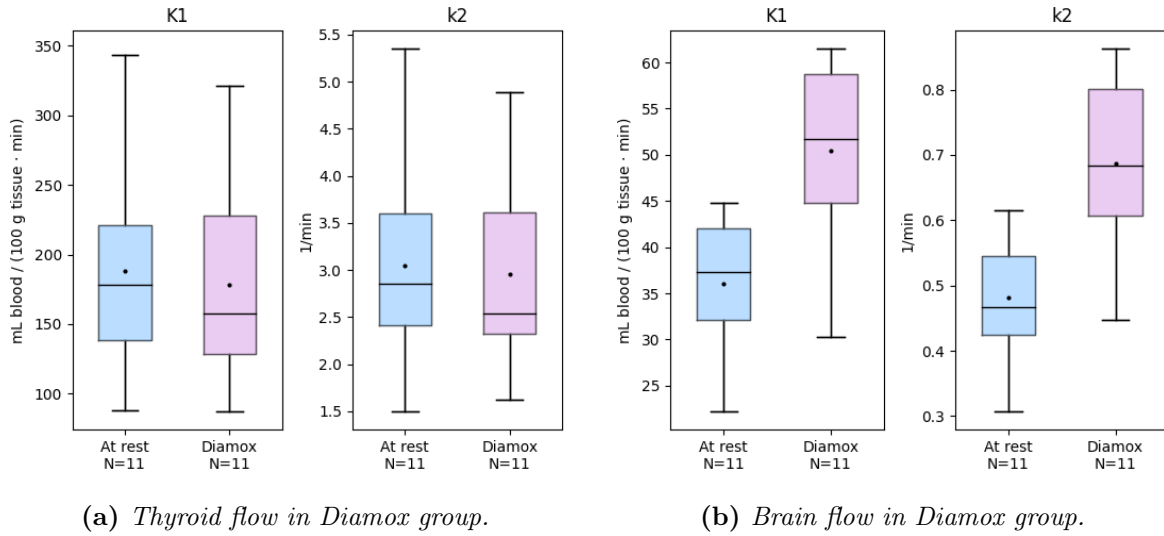


**Figure 4.6** – Comparison of the mean flow parameters  $K_1$  and  $k_2$  in the thyroid and brain between patients at rest and with Diamox. The black line and the black dot show the median and mean.  $N$  is the number of patients in each subgroup.

deviation between the two distributions, while larger p-values indicate a higher similarity between the two. To calculate the p-values we will be using Scipy’s T-test for two independent distributions, `scipy.stats.ttest_ind()`.

The p-values between the patients before treatment and after treatment is 0.00026 for  $K_1$  and 0.0019. Between the healthy controls and the patients before treatment, the p-values are 0.27 for  $K_1$  and 0.063 for  $k_2$ , while the p-values between the healthy controls and the patients after the treatment are 0.36 for  $K_1$  and 0.32 for  $k_2$ .

For the flow parameters in the brain of the same patients, the mean flow rates between the treatment changed  $-15\%$  for both  $K_1$  and  $k_2$ , although the p-values between these

**Table 4.2** – Overview of the results from flow modeling. The table lists the mean value for the flow parameters  $K_1$  and  $k_2$  in each of the subgroups.

	Thyroid flow		Brain flow	
	$K_1$ [mL/(100 g · min)]	$k_2$ [1/min]	$K_1$ [mL/(100 g · min)]	$k_2$ [1/min]
<b>Graves</b>				
• Before treatment	262 ± 15	4.6 ± 0.3	48 ± 7	0.6 ± 0.1
• After treatment	168 ± 13	2.7 ± 0.6	41 ± 7	0.5 ± 0.1
• Healthy control (HC)	220 ± 70	3.5 ± 1.0	46 ± 6	0.60 ± 0.09
<b>Diamox</b>				
• At rest	190 ± 80	3.0 ± 1.1	36 ± 7	0.48 ± 0.09
• With Diamox	180 ± 70	3 ± 1	51 ± 9	0.69 ± 0.13



distributions are relatively high of 26 % for  $K_1$  and 30 % for  $k_2$ . Again, the mean of the healthy controls lie in between before treatment and after treatment, with the difference between the mean of HC to the mean before treatment being +3.9 % for both  $K_1$  and  $k_2$ , and the change between HC and after treatment being  $-12\%$  for both  $K_1$  and  $k_2$ .

The p-values between the patients before treatment and the healthy controls are relatively high at 0.71 for  $K_1$  and 0.73 for  $k_2$ , while the p-values for the treated patients and the healthy controls are lower at 0.37 for  $K_1$  and 0.41 for  $k_2$ .

Figure 4.6 shows the mean flow parameters for patients before and after receiving the drug Diamox. In total 11 patients had scans at rest and with Diamox.

In contrast to the flow through the thyroid of the patients with Graves' disease, the change in flow rates for these patients from at rest to with Diamox is  $-5.1\%$  for  $K_1$  and  $-2.9\%$  for  $k_2$ , however, the p-values show large similarity between the two of 0.77 for  $K_1$  and 0.85 for  $k_2$ .

On the other hand, the difference in flow rate is larger for the brain between at rest and with Diamox, with  $K_1$  increasing by 40 % and  $k_2$  increasing by 43 %. The p-values between these two distributions are 0.00059 for  $K_1$  and 0.00039 for  $k_2$ , which is a sign of a more significant change.





# Discussion



From the delay maps in Figure 4.1 and the histograms in Figure 4.2, we have a visual overview of the temporal progression of the tracer – and thus also the blood carrying it – flowing through the bloodstream into organs and tissue.

For some of the organs, the standard deviations listed in Table 4.1 are quite large. However, as they in some cases do not describe Gaussian distributions, they should be interpreted with care in combination with the histograms of Figure 4.2. By comparing them visually to the histograms, we can describe the effect causing these standard deviations to be this large.

Firstly, the heart is divided into two halves: the right half which pumps deoxygenated blood to the lungs, and the left half which pumps the freshly oxygenated blood to the rest of the body. This gives the two distinct peaks around the lungs that subsequently lead to the larger range or standard deviation from the mean.

Secondly, the tracer appearance times in the aorta seem to be centered around a delay time of zero, but spread out over a range of  $\pm 2$ s. This is due to the fact that the input function is derived from the descending part of the aorta, as shown in Figure 3.2 on page 13, which receives blood later than than the ascending aorta or the aortic arch. We can easily calculate an estimate of how long time we expect it takes before blood reaches the descending part of the aorta. Ignoring age and health effects, we can assume the average blood velocity in the ascending aorta to be 6 cm/s [44] and the distance the blood has to travel before reaching the descending aorta, from which the input function is derived, to be 15 cm [45], we obtain a delay of  $\Delta t \approx 2.5$ s. This fits well with the histograms as well as the standard deviations listed in Table 4.1, containing delay times for selected organs.

Thirdly, the liver is spanning almost the full length of the histograms. Its width could partly be due to its supply of both venous and arterial blood [43], while the high activity in the early end of the histograms are likely to be from the patient breathing and the heart pumping, as a large part of the liver lies immediately beneath the lungs and heart. This can cause a part of heart and lungs to shift into the voxels that had been labeled as the liver from the MOOSE segmentation. Taking a closer look at the histograms, there exist small but discernible bumps on the histograms, being the heart beat, which match up between the heart and the liver, likely supporting this claim. Furthermore,



observing the whole-body delay maps, there is a perceptible area just underneath the heart with lower delay, which could be due to the same phenomenon, and be responsible for the high activity in the liver at the early end of the histograms.

As discussed in the introduction, water has an extraction fraction close to 1 [40] and DOTATATE has an extraction fraction that is very low [42], and assumed close to 0 for some tissue, due to it being a receptor based tracer, with FDG sitting in between these two with an extraction fraction of around 20% [41]. This also means that the signal to noise ratio is much lower for the patients receiving DOTATATE compared to water, which propagates through to the rest of the data, e.g. the delay map in Figure 4.1 for DOTATATE which has little to no signal in the patient's legs except for the relatively large illiac arteries, as well as displaying more noisy histograms. On the other hand, it is possible to discern the heartbeat especially well on the DOTATATE histograms in Figure 4.2c, in the histograms for the heart, lungs, aorta, liver and the brain. DOTATATE is not able to cross the blood-brain barrier [5, 6], and hence very little activity is observed in the brain, but this also results in the heart beat being more prevalent on the histograms in contrast to water, which diffuses through tissue without much trouble, which is therefore why we also observe a more smooth distribution in organ delays for this tracer.

Lastly, these values found for the delays of the organs are in line with what is expected with the delay times for the organs being within a few seconds of delay [46, 47].

The biggest challenge with creating a single-voxel resolution delay map is the noise associated with these small sets of data. And defining *when* the tracer appears in the tissue based on the TAC of a given voxel is not trivial either. Some TACs have a slow rising curve, i.e. tracer uptake in or supply to the tissue is slow and the value of the fitting parameter  $b$  is large, which means that the TAC around the onset is relatively flat and thus the uncertainty in the onset time will in turn be relatively large as well.

For the flow parameters in patients with Graves' disease, we can observe a significant change in the thyroid of around  $-40\%$  as a cause of the treatment, amounting to a change of  $\Delta K_1 = (-94 \pm 28) \text{ mL}/(100 \text{ g} \cdot \text{min})$  and  $\Delta k_2 = (-1.9 \pm 0.9)/\text{min}$ , with p-values of  $p \approx 0.002$  for both parameters. The flow in the brain had no significant change as a the effect of the treatment with p-values  $p > 0.25$ , meaning the treatment seems to be local to the thyroid. However, the patients prior to treatment seem to be more similar in flow in the brain with larger p-values of  $p \approx 0.7$  than after treatment, where the p-values are now  $p \approx 0.4$ . This discrepancy suggests that we might not yet be able to cast away the



hypothesis that the treatment is entirely local to the thyroid and that it does not affect the blood flow in the brain.

For the flow through the brain of the patients who received Diamox, we observe a significant change in flow rates of around +40% with p-values of  $p < 0.0006$ . On the other hand, there was no significant change in the thyroid of the same patients after receiving Diamox, as the p-values for  $K_1$  and  $k_2$  were around  $p \approx 0.8$ . This means that Diamox affects the brain and thyroid differently, with a large increase in flow through the brain, and no effect is observed for the thyroid.

Qualitatively, these changes in flow rates are expected, with the treatment of Graves' disease is meant to kill some of the thyroid cells [29], thus a decrease in flow should be observed. Additionally, Diamox is known to act as a vasodilate [31] and to increase the blood flow in the brain [48]. The behaviour of Diamox exhibiting an organ-specific effect on the blood flow rates is also suggested in a study on rabbits, which, in response to 12 mg/kg Diamox, saw *“an increase in blood flow of 82% in the brain [...], but no change in blood flow in the liver, stomach wall or abdominal muscle.”* [49]. The findings in this report on blood flow in the brain and in the thyroid support that the effect of Diamox on blood flow is organ-specific, with a high influence in the brain.

Finally, we can conclude that utilizing a single-voxel delay correction method when modeling the blood flow in organs with large regional differences in delay is important in order to achieve correct flow parameters, as is evident from Figure 4.4 on page 23, where the difference in modeled blood flow can be as large as about  $\Delta K_1 \sim 30 \text{ mL}/(100 \text{ g} \cdot \text{min})$  in the brain of patients receiving Diamox, with the mean flow being  $\overline{K_1^{brain}} \approx 50 \text{ mL}/(100 \text{ g} \cdot \text{min})$  in some cases.



# Future prospects

---



The next steps that can be taken with this project is to improve on the delay finding algorithm. Due to the low signal-to-noise ratio of single voxels, especially in some parts of muscle and skin tissue, the algorithm can have difficulty detecting which parts are noise and which are the signal. The algorithm already flags voxels that have bad fits and reruns these with nearest neighbor averaging to smoothen the TACs and gain more information based on the surrounding tissue while still keeping the time component intact. This has reduced the number of flagged voxels by around 90% in most cases, however, more can be done to improve on the accuracy of finding the onset of low signal-to-noise voxels.

Another aspect is the computation time. For whole-body PET scans it currently takes around 5 hours to complete when running the calculations in parallel on 50 CPUs (model name: Intel<sup>®</sup> Xeon<sup>®</sup> Gold 6346 CPU at 3.10 GHz) depending on the tracer used, the number of voxels included, as well as the temporal resolution of the TACs. From timing tests, it is apparent that upwards of 98% of the running time is used to fit the data. Reducing the number of data points used in the fit would improve the running time, but might inadvertently affect the accuracy of the results. Another possibility is to use a faster fitting algorithm than Scipy's `optimize.curve_fit()`, or even replace the fitting equation for a simpler one.

Since Rigshospitalet acquired its long-axial field of view scanner in 2021, the number of patients scanned in it is still fairly limited, and thus making accurate conclusions on a subset of these patients is difficult. More data is needed to be certain, however, from the results in this report we can already make preliminary conclusions.



# Conclusion

---

## 7

---

The algorithm outlined and developed in this report is able to robustly identify and find the delay times for single voxels as well as generating comprehensive delay maps for whole-body PET scans. It employs several techniques to mitigate the effects of the noise in the data and its influence on the fits. These include:

1. Summing the time activity curves (TACs) cumulatively,
2. Detecting plateaus caused by random noise spikes,
3. Fitting the data across several ranges, and choosing the best fit based on their  $R^2$ ,
4. And averaging a small volume of the nearest neighbors for TACs that were challenging to achieve good fits for, and where more information from the near tissue was needed.

Potential areas for improvements include studying the TACs of tissue with slow tracer uptake in detail, as these are the most challenging to define the onset due to their slow rising and often noisy behavior, as well as implementing a more noise resistant algorithm to help improve the accuracy of the delay maps even further.

Using scans from the newly acquired long-axial field-of-view PET/CT scanner at Rigshospitalet enabled us to model the kinetics of blood flow in multiple organs simultaneously, and together with the produced delay maps, it was possible to apply a single-voxel delay correction to the scans. Two groups of patients, diagnosed with either carotid stenosis or Graves' disease, were modeled prior to receiving a treatment as well as after, in order to observe if a possible change in blood flow occurred in either or both of the two organs of interest across all patients as a whole.

The findings would benefit from data from more patients, although, we are still able to make preliminary conclusions. These include that the treatment of Graves' disease is likely to be local to the thyroid, and that Diamox affects only the brain out of the two organs. Additionally, with the dynamic whole-body PET scans and the whole body delay maps, it is possible to model even more organs at a time.

Furthermore, the algorithm has demonstrated its effectiveness across three different tracers:  $[^{15}\text{O}]\text{H}_2\text{O}$ , the widely used radiotracer  $[^{18}\text{F}]\text{FDG}$ , as well as  $[^{64}\text{Cu}]\text{Cu}$ -



DOTATATE. These tracers together span a broad range of extraction fractions, in addition to their individual and unique physiological properties. Moreover, due to being applied to whole-body PET scans, the algorithm is also capable of finding delays in a variety of organs and tissues.

This can potentially help achieving more accurate flow rates in organs with large regional differences in delay and remove a bias that has so far been a part of the conventional method of delay correction.



# Bibliography

- [1] Dale L. Bailey et al. *Positron emission tomography*. Vol. 2. Springer, 2005.
- [2] Lale Kostakoglu, Harry Agress Jr., and Stanley J. Goldsmith. “Clinical role of FDG PET in evaluation of cancer patients”. In: *Radiographics* 23.2 (2003), pp. 315–340.
- [3] James W. Fletcher et al. “Recommendations on the use of  $^{18}\text{F}$ -FDG PET in oncology”. In: *Journal of Nuclear Medicine* 49.3 (2008), pp. 480–508.
- [4] Wolfgang A. Weber, Markus Schwaiger, and Norbert Avril. “Quantitative assessment of tumor metabolism using FDG-PET imaging”. In: *Nuclear medicine and biology* 27.7 (2000), pp. 683–687.
- [5] Andreas R. Haldemann et al. “Somatostatin receptor scintigraphy in central nervous system tumors: role of blood-brain barrier permeability”. In: *Journal of Nuclear Medicine* 36.3 (1995), pp. 403–410.
- [6] Punit Sharma et al. “Somatostatin receptor-based PET/CT of intracranial tumors: a potential area of application for  $^{68}\text{Ga}$ -DOTA peptides?” In: *American Journal of Roentgenology* 201.6 (2013), pp. 1340–1347.
- [7] Ismet Sarikaya et al. “Significance of splenic uptake on somatostatin receptor imaging studies”. In: *Nuclear Medicine Review* 21.1 (2018), pp. 66–70.
- [8] David J. Schlyer. “PET tracers and radiochemistry”. In: *ANNALS-ACADEMY OF MEDICINE SINGAPORE* 33.2 (2004), pp. 146–154.
- [9] Turku PET Centre, University of Turku. *Fick’s principle*. [https://vesoik.utugit.fi/petanalysis/ficks\\_principle.html](https://vesoik.utugit.fi/petanalysis/ficks_principle.html). [Accessed 17-May-2023].
- [10] Dengrong Jiang et al. “Normal variations in brain oxygen extraction fraction are partly attributed to differences in end-tidal  $\text{CO}_2$ ”. In: *Journal of Cerebral Blood Flow & Metabolism* 40.7 (2020), pp. 1492–1500.
- [11] P. Herscovitch, Joanne Markham, and M. E. Raichle. “Brain Blood Flow Measured with Intravenous  $\text{H}_2^{15}\text{O}$ : I. Theory and Error Analysis”. In: *Journal of Nuclear Medicine* 24.9 (1983), pp. 782–789.
- [12] Marcus E. Raichle et al. “Brain Blood Flow Measured with Intravenous  $\text{H}_2^{15}\text{O}$ : II. Implementation and Validation”. In: *Journal of Nuclear Medicine* 24.9 (1983), pp. 790–798.
- [13] Hiroshi Watabe et al. “Parametric imaging of myocardial blood flow with  $^{15}\text{O}$ -water and PET using the basis function method”. In: *Journal of Nuclear Medicine* 46.7 (2005), pp. 1219–1224.
- [14] Martin A. Lodge et al. “Reproducibility of tumor blood flow quantification with  $^{15}\text{O}$ -water PET”. In: *Journal of Nuclear Medicine* 49.10 (2008), pp. 1620–1627.
- [15] Society of Nuclear Medicine and Molecular Imaging. *SNMMI - Neuroendocrine Tumors*. [http://www.snmmi.org/Patients/Disease\\_Condition/Content.aspx?ItemNumber=13952](http://www.snmmi.org/Patients/Disease_Condition/Content.aspx?ItemNumber=13952). [Accessed 18-May-2023].



- [16] Andreas Pfeifer et al. “Clinical PET of neuroendocrine tumors using  $^{64}\text{Cu}$ -DOTATATE: first-in-humans study”. In: *Journal of Nuclear Medicine* 53.8 (2012), pp. 1207–1215.
- [17] Maurizio Conti and Lars Eriksson. “Physics of pure and non-pure positron emitters for PET: a review and a discussion”. In: *EJNMMI physics* 3 (2016), pp. 1–17.
- [18] Craig S. Levin and Edward J. Hoffman. “Calculation of positron range and its effect on the fundamental limit of positron emission tomography system spatial resolution”. In: *Physics in Medicine & Biology* 44.3 (1999), p. 781.
- [19] Paolo Zanotti-Fregonara et al. “Image-derived input function for brain PET studies: many challenges and few opportunities”. In: *Journal of Cerebral Blood Flow & Metabolism* 31.10 (2011), pp. 1986–1998.
- [20] Karmen K. Yoder. “Basic PET Data Analysis Techniques”. In: *Positron Emission Tomography*. Ed. by Sandro Misciagna. Rijeka: IntechOpen, 2013. Chap. 3. DOI: 10.5772/57126. URL: <https://doi.org/10.5772/57126>.
- [21] Lioe-Fee de Geus-Oei et al. “Comparison of image-derived and arterial input functions for estimating the rate of glucose metabolism in therapy-monitoring  $^{18}\text{F}$ -FDG PET studies”. In: *Journal of Nuclear Medicine* 47.6 (2006), pp. 945–949.
- [22] Paolo Zanotti-Fregonara et al. “Comparison of 3 methods of automated internal carotid segmentation in human brain PET studies: application to the estimation of arterial input function”. In: *Journal of Nuclear Medicine* 50.3 (2009), pp. 461–467.
- [23] Xiaoli Lan et al. “First clinical experience of 106 cm, long axial field-of-view (LAFOV) PET/CT: an elegant balance between standard axial (23 cm) and total-body (194 cm) systems”. In: *European Journal of Nuclear Medicine and Molecular Imaging* 48.12 (2021), pp. 3755–3759.
- [24] Jaroslaw Krejza et al. “Carotid artery diameter in men and women and the relation to body and neck size”. In: *Stroke* 37.4 (2006), pp. 1103–1105.
- [25] Elizabeth J. Li et al. “Efficient delay correction for total-body PET kinetic modeling using pulse timing methods”. In: *Journal of Nuclear Medicine* 63.8 (2022), pp. 1266–1273.
- [26] Hidehiro Iida et al. “Quantitation of regional cerebral blood flow corrected for partial volume effect using O-15 water and PET: I. Theory, error analysis, and stereologic comparison”. In: *Journal of Cerebral Blood Flow & Metabolism* 20.8 (2000), pp. 1237–1251.
- [27] Ian Alberts et al. “Long-axial field-of-view PET/CT: perspectives and review of a revolutionary development in nuclear medicine based on clinical experience in over 7000 patients”. In: *Cancer Imaging* 23.1 (2023), pp. 1–15.
- [28] Riemer HJA Slart et al. “Long axial field of view PET scanners: a road map to implementation and new possibilities”. In: *European journal of nuclear medicine and molecular imaging* 48.13 (2021), pp. 4236–4245.
- [29] National Institute of Diabetes and Digestive and Kidney Diseases. *Graves’ Disease - NIDDK*. <https://www.niddk.nih.gov/health-information/endocrine-diseases/graves-disease>. [Accessed 18-May-2023].
- [30] John Hopkins Medicine. *Carotid Artery Stenosis*. <https://www.hopkinsmedicine.org/health/conditions-and-diseases/carotid-artery-disease>. [Accessed 18-May-2023].





- [31] Hidehiko Okazawa et al. “Effects of acetazolamide on cerebral blood flow, blood volume, and oxygen metabolism: a positron emission tomography study with healthy volunteers”. In: *Journal of Cerebral Blood Flow & Metabolism* 21.12 (2001), pp. 1472–1479.
- [32] Hiroshi Watabe et al. “PET kinetic analysis—compartmental model”. In: *Annals of nuclear medicine* 20 (2006), pp. 583–588.
- [33] Turku PET Centre, University of Turku. *Compartmental models in positron emission tomography*. [http://www.turkupetcentre.net/petanalysis/model\\_compartmental.html](http://www.turkupetcentre.net/petanalysis/model_compartmental.html). [Accessed 18-May-2023].
- [34] Bailing Hsu. “PET tracers and techniques for measuring myocardial blood flow in patients with coronary artery disease”. In: *Journal of biomedical research* 27.6 (2013), p. 452.
- [35] Siemens Healthineers. *Biograph Vision Quadra*. <https://www.siemens-healthineers.com/en-us/molecular-imaging/pet-ct/biograph-vision-quadra>. [Accessed 18-May-2023].
- [36] Turku PET Centre, University of Turku. *imgflow - tpcplib*. <https://vesoik.utugit.fi/petanalysis/tpcplib/doc/imgflow.html>. [Accessed 20-April-2023].
- [37] Turku PET Centre, University of Turku. *fit\_h2o - tpcplib*. [https://vesoik.utugit.fi/petanalysis/tpcplib/doc/fit\\_h2o.html](https://vesoik.utugit.fi/petanalysis/tpcplib/doc/fit_h2o.html). [Accessed 20-April-2023].
- [38] Turku PET Centre, University of Turku. *TPC - PET data analysis and modelling*. <http://www.turkupetcentre.net/petanalysis/>. [Accessed 20-April-2023].
- [39] Lalith Kumar Shiyam Sundar et al. “Fully Automated, Semantic Segmentation of Whole-Body <sup>18</sup>F-FDG PET/CT Images Based on Data-Centric Artificial Intelligence”. In: *Journal of Nuclear Medicine* 63.12 (2022), pp. 1941–1948.
- [40] Anne Bol et al. “Direct comparison of [<sup>13</sup>N] ammonia and [<sup>15</sup>O] water estimates of perfusion with quantification of regional myocardial blood flow by microspheres.” In: *Circulation* 87.2 (1993), pp. 512–525.
- [41] Marc C. Huisman et al. “Cerebral blood flow and glucose metabolism in healthy volunteers measured using a high-resolution PET scanner”. In: *EJNMMI research* 2.1 (2012), pp. 1–9.
- [42] Salih Özgüven et al. “Physiological Biodistribution of 68 Ga-DOTA-TATE in Normal Subjects.” In: *Molecular Imaging & Radionuclide Therapy* 30.1 (2021).
- [43] Yuji Itai and Osamu Matsui. “Blood flow and liver imaging.” In: *Radiology* 202.2 (1997), pp. 306–314.
- [44] Leidulf Segadal and Knut Matre. “Blood velocity distribution in the human ascending aorta.” In: *Circulation* 76.1 (1987), pp. 90–100.
- [45] Charles T Dotter, DOUGLAS J ROBERTS JR, and Israel Steinberg. “Aortic length: angiographic measurements”. In: *Circulation* 2.6 (1950), pp. 915–920.
- [46] H. Iida et al. “Evaluation of regional differences of tracer appearance time in cerebral tissues using [<sup>15</sup>O] water and dynamic positron emission tomography”. In: *Journal of Cerebral Blood Flow & Metabolism* 8.2 (1988), pp. 285–288.
- [47] K. Herholz et al. “Regional cerebral blood flow measurement with intravenous [<sup>15</sup>O] water bolus and [<sup>18</sup>F] fluoromethane inhalation.” In: *Stroke* 20.9 (1989), pp. 1174–1181.



Frederik Bay Nielsen  
*University of Copenhagen*  
May 22<sup>nd</sup>, 2023

*BIBLIOGRAPHY*

- [48] Sissel Vorstrup, Leif Henriksen, Olaf B Paulson, et al. “Effect of acetazolamide on cerebral blood flow and cerebral metabolic rate for oxygen.” In: *The Journal of clinical investigation* 74.5 (1984), pp. 1634–1639.
- [49] Kenji Taki et al. “Acetazolamide-induced increase in blood flow to rabbit organs is confirmed using colored microspheres”. In: *Heart and Vessels* 13 (1998), pp. 63–67.